Random Walk and Graph Cut for Co-Segmentation of Lung Tumor on PET-CT Images

Wei Ju, Deihui Xiang, Bin Zhang, Lirong Wang, Ivica Kopriva, *Senior Member, IEEE*, and Xinjian Chen*, *Senior Member, IEEE*

Abstract—Accurate lung tumor delineation plays an important role in radiotherapy treatment planning. Since the lung tumor has poor boundary in positron emission tomography (PET) images and low contrast in computed tomography (CT) images, segmentation of tumor in the PET and CT images is a challenging task. In this paper, we effectively integrate the two modalities by making fully use of the superior contrast of PET images and superior spatial resolution of CT images. Random walk and graph cut method is integrated to solve the segmentation problem, in which random walk is utilized as an initialization tool to provide object seeds for graph cut segmentation on the PET and CT images. The co-segmentation problem is formulated as an energy minimization problem which is solved by max-flow/ min-cut method. A graph, including two sub-graphs and a special link, is constructed, in which one sub-graph is for the PET and another is for CT, and the special link encodes a context term which penalizes the difference of the tumor segmentation on the two modalities. To fully utilize the characteristics of PET and CT images, a novel energy representation is devised. For the PET, a downhill cost and a 3D derivative cost are proposed. For the CT, a shape penalty cost is integrated into the energy function which helps to constrain the tumor region during the segmentation. We validate our algorithm on a data set which consists of 18 PET-CT images. The experimental results indicate that the proposed method is superior to the graph cut method solely using the PET or CT is more accurate compared with the random walk method, random walk co-segmentation method, and non-improved graph cut method.

Index Terms—Image segmentation, interactive segmentation, graph cut, random walk, prior information, lung tumor, positron emission tomography (PET), computed tomography (CT).

W. Ju, D. Xiang, L. Wang, and X. Chen are with the School of Electronic and Information Engineering, Soochow University, Suzhou 215123, China (e-mail: yehesu@163.com; xiangdehui@suda.edu.cn; wanglirong@ suda.edu.cn; xjchen@suda.edu.cn). *(Wei Ju and Deihui Xiang contributed equally to this work.)*
B. Zhang is with the First Affiliated Hospital of Soochow University, Suzhou 215123, China (e-mail: zbnuclmd@126.com).
I. Kopriva is with the Division of Laser and Atomic Research and Development, Ruder Bošković Institute, Zagreb 10000, Croatia (e-mail: ikopriva@irb.hr).

I. Introduction

LUNG CANCER is the leading cause of cancer-related deaths worldwide in both men and women [1]. The combination of chemotherapy and radiotherapy is a commonly recommended standard curative approach in non-small cell lung cancer (NSCLC) which is a major kind of lung cancer [2]. Currently, preoperative imaging is recommended for the malignancy grade of non-invasive lung tumors before treatments are provided [3]–[5]. ^{18}F-deoxyglucose (FDG) uptake is related to many biological processes, including glucose metabolism and hypoxia [6]. Therefore, FDG Positron Emission Tomography (PET) is often used to stage NSCLC in clinic [7]. However, it is a non-trivial task for cancer assessment and treatment planning, due to the variability and diversity of medical images [8], [9]. In PET images, the diseased areas, such as tumor and inflammation, appear as 'hot' areas reflecting high contrast to the normal surrounding tissues. The high contrast in PET images makes it easy to distinguish the malignant areas from the normal tissues and gives the observer a distinct visualization which reduces the observer variability [10]. However, due to the low spatial resolution of PET [11], the target boundary definition is poor and fuzzy [see Fig.1(a)]. Thus, accurate tumor segmentation using PET only is problematic. Computed Tomography (CT) images have high spatial resolution and provide detailed anatomical information, yet lacking metabolic information. Lack of physiological information in CT makes it difficult to distinguish between the lesion and the normal tissues because the tumor intensity is similar to the surrounding tissues [12] [see Fig.1(b)]. With the introduction of multi-modality imaging technologies, integrated PET/CT scanners can provide co-registered FDG-PET and CT images, make it possible to acquire both anatomic and functional images of the whole patient in one single procedure [13]. Many studies indicated that the combination of PET and CT images produce a more consistent tumor volumes [14]–[16]. Therefore, PET-CT gained a lot of attention in the field of both clinic and image processing and has become a standard method for tumor delineation and cancer assessment [17].

Although PET-CT images have been widely used in clinic, automatic segmentation on PET-CT images is still a challenging task. The existing methods working for PET-CT [18]–[21] have an underlying assumption that the tumor volume is identical on PET and CT, attempting to get one tumor contour from PET and CT two modalities. However, as PET and CT convey different information, which is not always
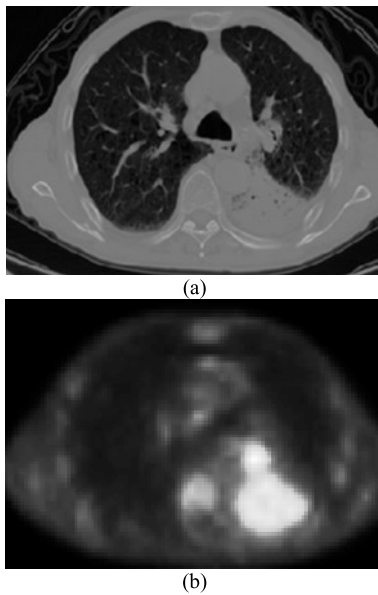
Fig. 1. PET and CT images. (a) One slice of a CT image. (b) The corresponding PET image.

complementary, but sometimes contradictory, the tumor volume may be different on PET and CT [22]. In this work, we strive to segment tumor volumes simultaneously by taking the advantages from two modalities, the superior contrast of PET images and superior spatial resolution of CT images and get two different tumor volumes. Our method is based on Boykov's graph cut method [23]–[27] and Leo Grady's random walk method [28], [29]. Both of the methods treat the image as a graph and minimize energy functions on the constructed graph to produce an optimal segmentation. In both methods, a weighted graph is constructed. Nodes of the graph correspond to voxels in image and edges are placed between nearby voxels [30]. The edge weights are determined by the image intensity. We incorporate the two methods together by utilizing random walk as an initial preprocessor and graph cut as a co-segmentation problem solver. Random walk is utilized to provide initial lesion detection on PET, which will be used as object seed sets for PET and CT, and also as an initial shape prior for tumors in CT images. The co-segmentation problem is formulated as an energy minimization problem. As a graph-based method, the performance of the graph cut method is determined by the energy function. We proposed a novel energy function which is well adjusted to the characteristic of PET and CT images. The energy function for both PET and CT segmentation has two terms, region term and boundary term. For PET, the region cost consists of three different kinds of feature extracted from PET images, a data term based on the SUV distribution, a downhill feature and a three-dimensional (3D) derivate feature. The SUV distribution feature helps to solve the problem of heterogeneity in PET images. The downhill feature based on the analysis of tumor characteristics in PET would help extract the ambiguous area of tumors, which has a similar intensity distribution to non-tumor regions such as heart and liver. The 3D derivative feature which is formulated using the Hessian matrix combined with Gaussian functions is able to enhance

the tumor objects. For CT segmentation, the region term is the incorporation of a data cost function and a shape penalty term, which utilizes shape prior information to limit the tumor area. The boundary term for both PET and CT segmentation is based on the gradient information of the images. To get consistent results between PET and CT, a context term which penalizes the difference between them is added to the energy. The solution with respect to energy function minimization will be achieved in a polynomial time by computing maximum flow in the constructed graph [25].

The rest of the paper is organized as follows. In section II, we give a brief review on tumor segmentation using PET and CT images and characterize the novelties of our approach. In section III, we describe the framework of our method and give the details about each part, including the description of the energy function design. Section IV gives the detailed description of the experiments and presents the experimental results. Finally, in section V, we draw the conclusion and section VI gives the discussion of our work and the future improvements.

II. Related Work

PET images have been actively in use for tumor delineation in clinical radiotherapy applications due to their high contrast to non-tumor tissues. In the literature, SUV thresholding was widely used. Erdi *et al.* applied a fixed threshold value of 36%–44% of the maximum SUV derived from the phantom experiments to PET images in order to determine the regions of primary or metastatic lung lesions [31]. In their phantom study on moving tumors, Caldwell *et al.* also used a threshold of 15% of the maximum in order to detect the true extension of the target volume [32]. Drever *et al.* also proposed a threshold segmentation method based on local contrast to accurately delineate PET target cross sections using well-defined cylindrical and spherical volumes [33]. Then, they also carried out a phantom study employing spherical targets to determine local threshold value between target and background, and fit functions to this data in order to construct a local contrast based iterative threshold segmentation algorithm [34]. Jentzen *et al.* also proposed an iterative thresholding method which had good performance in dealing with indistinct nature of tumor boundary have been extensively developed [35]. Brambilla *et al.* used multiple linear regression models to study the dependence of the percentage threshold used to define the boundaries of FDG positive tissue on emission scan duration and activity at the start of acquisition or different target sizes and target-to-background ratios [36] Nehmeh *et al.* developed an iterative method based on Monte Carlo to determine the optimum threshold value [37]. Similar to the thresholding methods, some features derived from SUV were introduced. Wong *et al.* used shape and magnitude to classify a number of time-activity curves (TACs) into a smaller number of distinct characteristic classes that are mutually exclusive so that the tissue TACs within a cluster are similar to one another but are dissimilar to those drawn from other clusters [38]. Geets *et al.* computed the gradient intensity of each voxel in PET images, and then detected crest using watershed transform. In order to obtain final tumor segmentation, they

used a hierarchical clustering algorithm by constructing a dissimilarity dendrogram and collecting all patches/watersheds sharing a similar activity level [39] Wanet *et al.* also used a gradient-based approach for denoised and deblurred PET images and fixed and adaptive thresholding method to compute gross target volume (GTV) [40]. Besides, additional features were also incorporated. Spatial information related to the voxel position in the PET data in a flexible manner was obtained from anisotropic diffusion filtering such that fuzzy C-means FCM clustering algorithm can be optimized [41]. In [42], horizontal, vertical, and diagonal features for each slice were produced using Haar wavelet transform and were used in artificial neural network for classifying and quantifying tumors. Texture-based features were also introduced to reflect the underlying spatial variation and heterogeneity of voxel intensities within tumors [43]–[45]. More complex methods were developed and applied to lung tumor segmentation in PET images. Guan *et al.* proposed a body-section labeling method based on spatial Hidden-Markov Models (HMM) and combined a competition diffusion segmentation algorithm and a recursive intensity mode seeking algorithm to detect tumor hotspot region [46] Montgomery *et al.* introduced expectation maximization based mixture modeling using a k-means clustering method, and then used a multiscale Markov model to refine segmentation automatically [47]. The distribution of SUV in a PET image was expressed as a mixture of Gaussian densities representing different classes to obtain the tumor volume with user interaction [48]. Ballangan *et al.* employed the relationship between SUV and its gradient magnitude to formulate tumor-customized downhill model and used a tumor-customized downhill algorithm to detect tumor boundary [49] Dewalle-Vignion *et al.* integrated the maximum intensity projection algorithm to handle consistent information from high PET images and developed a fuzzy set theory-based algorithm to utilize uncertainty between healthy tissues and tumors [50] Recently, graph based methods have attracted a lot of attention due to their good performance in image segmentation. Bagci *et al.* demonstrated the effectiveness of segmenting lung tumor on PET images using random walk algorithm [51]. Cherry *et al.* showed how to extract heart, liver and regions effectively which have similar uptake value to lesions by merging a novel monotonic downhill function with the conventional graph cut energy regularization [52].

Apart from the detection of pulmonary lesions in PET images described above, many researchers also tried to detect pulmonary nodules in CT images due to the nature of the CT scanners. Kuhnigk *et al.* initially performed a region growing algorithm with a fixed lower threshold starting from the seed point. Then, they combined a morphological opening operation based on automated determination of an optimal erosion strength and a chest wall separation procedure [53], In Wu's work [54], they used a conditional random field model incorporating texture features, gray-level, shape, and edge cues to segment lung nodules. Tao *et al.* presented a multi-level statistical learning-based framework for automatic detection and segmentation of ground glass nodules in lung CT images [55]. Gu *et al.* developed a single click ensemble segmentation approach [56].

However, these methods only conducted on single modality. Due to physically limited spatial resolution and lack of anatomical information in PET images while low contrast in CT images, many developers recently attempted to integrate PET and CT images, striving to achieve more precise lesion detection and delineation. Erdi *et al.* used a semi-automatic method to analyze lung tumors. They delineated prospectively planning target volume (PTV), gross target volume (GTV) and normal organs in CT images. The PTV and GTV were then modified using the registered PET emission images [10]. Jafar *et al.* used an iterative optimal thresholding algorithm to extract the lungs out of the whole-body in PET/CT images and applied multiple thresholding procedure with volume criterion to detect the tumors according to the PET/CT volumes in equally spaced gray levels [57] Ballangan *et al.* used a fixed threshold based region growing for initial lung segmentation, and then aligned the healthy lung template to the patient image volumes to lung and tumors [58]. Guo *et al.* used a joint posterior probability distribution of observed features in the fuzzy MRF model to segment lung tumors from PET-CT images [59]. Bagci *et al.* proposed an automatic random-walk-based segmentation method combining PET, CT and MRI modalities by the hyper graph construction [18]. Han *et al.* developed an optimal graph-based co-segmentation method with the establishment of an arbitration graph mechanism, encoding the characterized information of PET and CT images and the context information between them [20]. Based on Han's method, Song *et al.* reduced the size of the constructed graph in Han's paper from three sub-graphs to two and tried to obtain two different tumor contours on PET and CT [22].

Our work is motivated by Song's method [22]. We both formulate the co-segmentation problem as a labeling of Markov Random Field (MRF) on the constructed graph with PET and CT images. Compared to Song's method, the innovation in our work is the combination of random walk and graph cut and the introduction of a novel energy representation. The random walk technique is utilized to provide initial hot spot detection which is treated as object seed points required by graph cut. As we know, the graph cut algorithm has small cut and shrinking problem in noisy images if a small number of seeds are used. The prior tumor appearance provided by random walk can avoid the small cut problem happening and reduce the user's intervention. Since random walk is more efficacious in handling ambiguities among object boundaries, the initial detection by random walk will capture weak boundaries of the target regions. Moreover, the downhill term which is integrated into the PET energy function has great contributions to producing accurate lesion segmentation from PET images. The downhill term helps to identify the location of the tumor and extract the ambiguous area which has similar intensity to the tumor. The 3D derivative feature enhances the tumor structures and weakens the background field.

III. METHODS

Our proposed algorithm is based on two graph-based methods, random walk (RW) and graph cut (GC). Random walk is an initial preprocessor for PET, providing basic tumor

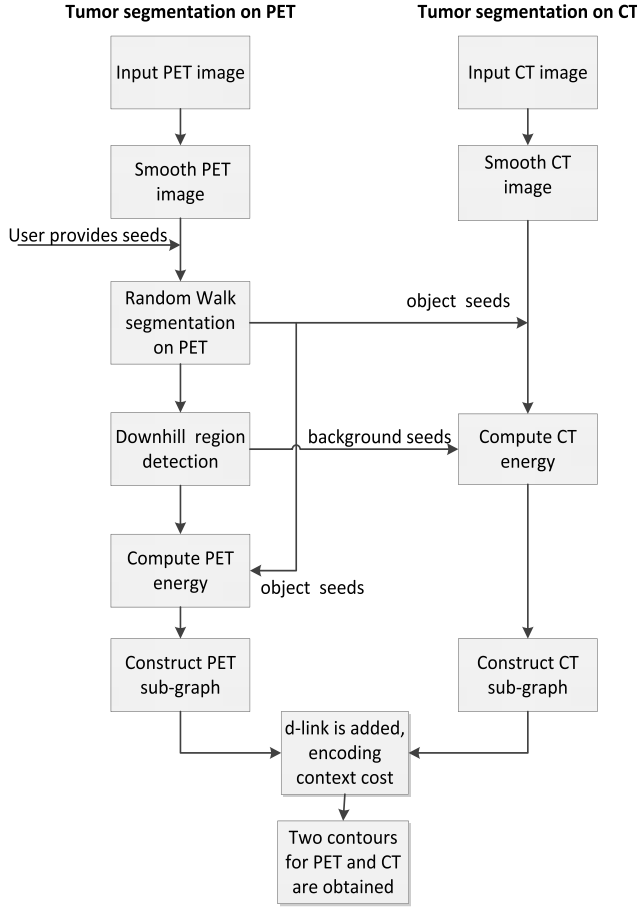**Tumor segmentation on PET**   **Tumor segmentation on CT**

Fig. 2.   Flowchart of the algorithm.

appearance which is used as object seed points for PET and CT. Then the task of simultaneous segmentation is formulated as an energy minimization problem on graphs corresponding to PET and CT images. The graph is constructed involving two sub-graphs, one for PET and one for CT. Inter-graph arcs called *d-link* are added to connect correspondent nodes of the two sub-graphs. For each sub-graph, a novel energy expression is designed. The inter-graph arcs enforce context information between PET and CT, enabling target contours to follow salient features of each modality [22].

The flowchart of the proposed algorithm is shown in Fig.2. First, anatomical and functional image are filtered by gradient anisotropic diffusion filter which is used to smooth images but preserve the edge. Then random walk is conducted on PET images and the initial results are obtained. Downhill region is detected on PET images and the area outside the downhill region is used as background seed set for CT segmentation. PET energy and CT energy and context cost is computed, encoded on the constructed graph. The entire energy is minimized by solving a max-flow/min-cut problem in the constructed graph in a polynomial time [25].

A. Pre-Processing

In the preprocessing step, PET images are registered and upsampled using a linear interpolator to obtain one-to-one

voxel correspondence between the CT images. As random walk is an interactive method, the object and background seeds are needed for guidance of the desired content to be extracted. In this work, seeds are selected from the tumor region by simulating Monte-Carlo. The seed number is set as five on each slice with tumor.

B. Random Walk for Tumor Segmentation on PET Images

Random walk is a graph-based segmentation approach. In this section, we give a detailed introduction of random walk.

Assume a graph G is connected and undirected, we represent graph G as $G = (V, E)$ with vertices $v \in V$ and edges $e \in V \times V$. e_{ij} is an edge connecting node v_i and its neighborhood v_j with a weight w_{ij}. The vertices in the graph can be divided into two sets, V_M and V_U, such that $V_M \cup V_U = V$ and $V_M \cap V_U = \emptyset$. V_M is a labeling seed set which is defined by users and V_U contains all unknown nodes. The segmentation problem is to find appropriate labeling for the unknown nodes. A weighting function maps a change in image intensity to edge weight corresponding to the likelihood that a random walker will cross that edge. The weighting function we employed is the typical Gaussian function derived from the suggestion in (Grady, 2006) [28].

$$w_{ij} = \exp(-\beta(g_i - g_j)^2), \qquad (1)$$

where g_i indicates the intensity at voxel i, the value β represents weighting parameter. It has been demonstrated previously that the desired probabilities the random walker passing through the edge has the same solution as the combinatorial Dirichlet problem [28]. The formulation of Dirichlet integral is stated as:

$$D[x] = \frac{1}{2}x^T L x = \frac{1}{2} \sum_{e_{ij} \in E} w_{ij} \left(x_i - x_j\right)^2, \qquad (2)$$

where x denotes the probability at each voxel, L represents the combinatorial Laplacian matrix. The matrix L is defined as

$$L_{ij} = \begin{cases} d_i & if \ i = j, \\ -w_{ij} & if \ v_i \ and \ v_i \ are \ adjacent \ nodes, \\ 0 & otherwise \end{cases} \qquad (3)$$

where L_{ij} is indexed by vertices v_i and v_j, d_i is the degree of a vertex for all edges e_{ij} incident on v_i and has the definition as: $d_i = \sum w(e_{ij})$.

After the probability x at each voxel is obtained, a threshold is set to segment the tumor from the image. If the probability of one voxel is larger than the threshold, it belongs to the tumor. Otherwise, it belongs to the background. And we use morphological operations of erosion followed by dilation approaches to deal with the isolated voxels. The segmentation results obtained from the random walk method are used as the foreground seeds for graph cut method and also as shape prior information for the shape penalty function term in the CT energy function.

→ **t-links** encode regional information
→ **n-links** encode neighboring information
→ **d-links** encode context term penalizing the
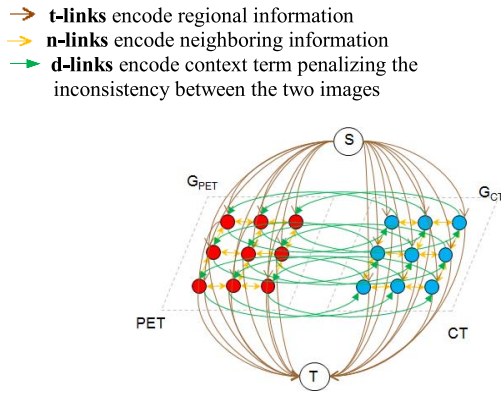   inconsistency between the two images

Fig. 3.   The constructed graph with two sub-graphs G_{PET} and G_{CT} and d-link arcs encoding the context penalties.

C. Graph Cut for Co-Segmentation of Tumor on PET-CT Images

In this section, we will introduce how to segment tumor concurrently on PET and CT images using graph cut technique. The rationale is to formulate the segmentation problem as finding the labeling by energy minimization. The foreground seeds are derived from the initial lesion appearance detected by random walk and the feature of tumor adjusted to the PET energy function will help to identify the background regions. The solution will be achieved by solving a maximum flow problem in low-order polynomial time [25].

1) Graph Construction: Two sub-graphs G_{PET} for PET, G_{CT} for CT, and a connector which is called *d-link* constitutes the whole graph. The graph is shown in Fig.3. For each voxel $u \in G_{PET}$, $u' \in G_{CT}$ is the corresponding voxel in CT. The intensity value for voxel u(u') is noted by g_u ($g_{u'}$). Label f indicates that the voxel belongs to the target object ($f = 1$) or to the background ($f = 0$). Each sub-graph contains *n-links* and *t-links*, encoding the neighboring costs and regional costs. For PET segmentation, the energy function E_{PET} has a region cost and a smoothness cost. For the segmentation of CT, the energy term E_{CT} has the same ingredient for that in PET. *d-links* are additional inter-graph arcs which connect the voxels u in G_{PET} and the corresponding u' in G_{CT}, enforcing the context information between PET and CT. The context cost $E_{context}$ penalizes the inconsistence segmentation between PET and CT. The total cost function is defined in the following way.

$$E(f) = E_{PET}(f) + E_{CT}(f) + E_{context}(f), \qquad (4)$$

The co-segmentation is done on a full 3D volume. Our goal is to minimize the energy such that the optimal segmentation of PET-CT images is attained.

2) Cost Function for PET: To introduce our energy function, we start with the expression of PET cost function. The cost has a region term which consists of a SUV cost, a downhill cost, a 3D derivative cost and a boundary term. The SUV term $R_u(f_u)$ is based on the SUV distribution of PET images. The downhill term $D_u(f_u)$ is adjusted to the downhill feature of tumor on PET and the 3D derivative cost $F_u(f_u)$ utilizes the derivative feature of PET images. The boundary

term $B_{uv}(f_u, f_v)$ is based on the gradient information of the image. The energy function for the segmentation of PET is defined as follows.

$$\begin{aligned} E_{PET}(f) = &\sum_{u \in G_{PET}} \lambda_1 \cdot (R_u(f_u) + F_u(f_u) + D_u(f_u)) \\ &+ \sum_{(u,v) \in N_{PET}} \lambda_2 B_{uv}(f_u, f_v), \end{aligned} \qquad (5)$$

where N_{PET} denotes the neighboring relationship between voxels in PET graph G_{PET}. λ_1, λ_2 is the scaling constant which maintains the role of the region term and the boundary term. The detailed definition of each function term is presented as follows.

a) Data term: The region term $R_u(f_u)$ is the likelihood assigning label f_u to the voxel u. Instead of user identifying object seeds manually, the pre-segmented tumor appearance (which is conducted by random walk) is considered as target regions desired to be segmented. Therefore, for every voxel inside the target regions, $R_u(f_u = 1) = 0$ and $R_u(f_u = 0) = +\infty$. In this paper, there is no need to define the background seed sets for PET segmentation because a downhill cost we defined is able to extract the ambiguous area which has the similar SUV to the tumor. For the spheres outside the initially identified region, it is important to note that the tumor may contain regions of necrosis or cystic change such that FDG uptake throughout the tumor is heterogeneous. To solve the problem of heterogeneity, the cost function based on the prior knowledge and the feature of SUV distribution of tumor is designed. Based on prior knowledge, it is highly possible that the voxels having SUV higher than 50% of maximum SUV belong to the tumor. We denote S_{MAX} the maximum SUV [60]. For every voxel with a lower value than 15% of S_{MAX}, it is more likely belonging to the background. The function is defined as:

$$R_u(f_u = 1)$$
$$= \begin{cases} T_{max} & if \ S(u) < S_L \\ T_{max} \cdot (1 - \dfrac{1}{1 + \exp(-(S(u) - \frac{S_L}{S_H} - S_L - \varphi)/\gamma)/\gamma}) \\ & if \ S_L < S(u) < S_H \\ 0 & if \ S(u) > S_H, \end{cases} \qquad (6)$$

$$R_u(f_u = 0) = T_{max} - R_u(f_u = 1), \qquad (7)$$

where T_{max} is the maximum region cost allowed; $S_H = 50\% \cdot S_{MAX}$ and $S_L = 15\% \cdot S_{MAX}$ are the higher and lower threshold value. γ is the parameter controlling the curvature of the function. φ controls the center point of the function. We employ the function instead of the linear function because it is monotonically increasing, more versatile and more robust to the heterogeneity.

b) 3D Derivative feature: The basic idea of the 3D derivative cost is to characterize the tumor based not only on its intensity values but also its local intensity structures. Therefore we design the 3D derivative cost which is based on the gradient vector and Hessian matrix of the volume intensity function combined with isotropic Gaussian functions to enhance the tumor structures [61]. The target lesion object

can be regarded as blob-like structures. So the derivative cost is devised to enhance the local blob-like structures and eliminate the ambiguous areas.

Let $g(\mathbf{x})$ be an intensity function of an image, $\mathbf{x} = (x, y, z)$. The second-order approximation of g(x) around x_0 can be formulated as follows:

$$g_{II}(x) = g(\mathbf{x_0}) + (\mathbf{x} - \mathbf{x_0})^T \nabla g_0$$
$$+ \frac{1}{2}(\mathbf{x} - \mathbf{x_0})^T \nabla^2 g_0 (\mathbf{x} - \mathbf{x_0}), \qquad (8)$$

where $g(x_0)$, ∇g_0 and $\nabla^2 g_0$ represent the original image intensity, the gradient vector and the Hessian matrix at x_0.

The gradient vector is defined as:

$$\nabla g = (g_x, g_y, g_z), \qquad (9)$$

where the partial derivatives of $g(x)$ are represented as $g_x = \frac{\partial g}{\partial x}$, $g_y = \frac{\partial g}{\partial y}$ $g_z = \frac{\partial g}{\partial z}$. And gradient magnitude is given by $|\nabla g| = \sqrt{g_x^2 + g_y^2 + g_z^2}$. g and $|\nabla g|$ are two intuitive feature measurements of 3D local intensity structures which representing the intensity and the edge length of the 3D structures.

The Hessian matrix is given by

$$\nabla^2 g = \begin{bmatrix} g_{xx} & g_{xy} & g_{xz} \\ g_{yx} & g_{yy} & g_{yz} \\ g_{zx} & g_{zy} & g_{zz} \end{bmatrix}, \qquad (10)$$

where the partial second-order differentiation is interpreted as a convolution with derivatives of Gaussians [61]:

$$g_{xx} = \frac{\partial}{\partial x}\left(\sigma_1^\delta g(x) * \frac{\partial}{\partial x} G(x, \sigma_1)\right), \qquad (11)$$

$$G(x, \sigma_1) = \frac{1}{\sqrt{2\pi\sigma_1^2}} e^{-\frac{\|x\|^2}{2\sigma_1^2}}, \qquad (12)$$

where σ_1 is a Gaussian parameter which controls the response of the derivative function to the specific local tumor structures and δ is a parameter. Since the tumor is anomalous, tumor structures can exist at various scales. In order to make filter responses tunable to a width of interest, the Hessian matrix is combined with Gaussian convolution. By adjusting the standard deviation of Gaussian convolution, local structures with a specific range of widths can be enhanced. The filter responses decrease as σ_1 increases unless appropriate normalization is performed. Let the eigenvalues of $\nabla^2 g$ be $\alpha_1, \alpha_2, \alpha_3$ ($\alpha_1 \leq \alpha_2 \leq \alpha_3 \leq 0$). These eigenvalues are combined and associated with the intuitive measures g and $|\nabla g|$. The tumor structure can be identified by using the eigenvalues $|\alpha_1|$ which gives the maximum second-derivative value measuring the similarity to the tumor structures. The 3D derivative cost is defined as follows.

$$F_u = |\alpha_1| \cdot T_{\max}, \qquad (13)$$

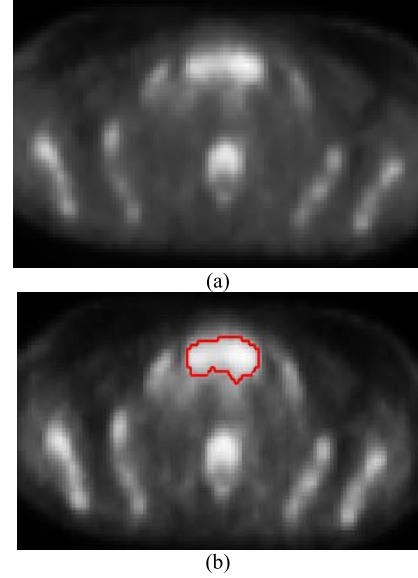where $T_{\max}$ is the maximum region cost allowed.

Fig. 4. One example slice of a downhill region image (a) original PET image (b) downhill region image overlaid on the original PET image. The curve in red is detected by the downhill function which shows that the feature effectively extracted the spine field which has a similar intensity to the tumor.

c) Downhill term: The proposed novel downhill cost which is integrated into the energy function is based on the analysis of tumor activity on PET. On PET images, the lesions with high metabolism have high uptake, so the tumor is clearly identified. However, the transition from the tumor SUV to the background SUV is gradual. Thus, the SUV of a homogeneous tumor is considered as 3D decreasing monotonically [49]. It means that within the tumor region, the further a voxel from the maximum intensity site of the tumor, the lower the SUV. So if a voxel has a high SUV and the distance to the maximum point is within the limited scale, the possibility that it belongs to the tumor region is higher. The algorithm of the downhill term is described in Algorithm 1.

Therefore, the downhill region has the following formulation:

$$V_D = \left\{ \begin{matrix} u| \; if \; SUV(u) > \mu SUV_{max} \; and \; d < d_0 \\ d_0 = \|x_u - x_{max}\| \; if \; SUV(u) < \mu SUV_{max} \end{matrix} \right\}, \qquad (14)$$

where x_{max} is the coordinate of the voxel with maximum SUV within the tumor domain, x_u, the coordinate of a voxel u. $\|\cdot\|$ is the Euclidean distance. μ is a parameter which controls the threshold value and limits the growth of the downhill region. V_D is the region which is detected by the downhill formulation.

The downhill cost is as follows:

$$D_u = \begin{cases} 0 & u \in V_D \\ T_{max} & otherwise, \end{cases} \qquad (15)$$

where T_{max} is the maximum region cost allowed.

Another advantage of the downhill region detection is that the voxels in the exterior of the downhill region can be considered as background seeds for CT segmentation. Fig.4(b) shows one slice with the detected downhill region.

Algorithm 1 Downhill Region Detection

Input: PET image and the prior segmentation result produced by random walk technique

Begin

1) Find SUV_{max}. Within the tumor area which is specified by random walk, the voxel with maximum SUV in PET images is found.

2) Calculate d_0. Starting at the maximum voxel, searching the neighboring voxels, if the SUV of the voxel is less than the thresholds, the distance from the current point to the maximum point is computed, denoted by d_0. The computation of d_0 is to limit the scale of the lesion field which effectively extracts the liver, heart and the ambiguous area which has similar intensity to the tumor.

    $if\ SUV(u) < \mu SUV_{max}, d_0 = \|x_u - x_{max}\|$

3) Detect the downhill region V_D. If the voxel satisfies the following condition, then it is specified as the points in the downhill region.

    $if\ SUV(u) > \mu SUV_{max}\ and\ d < d_0\ ,\ u \in V_D\ (\ d = \|x_u - x_{max}\|)$

End

Output: The detected downhill region V_D

(a)

(b)

Fig. 5.   One example slice of a cost image for region term in (a) PET image (b) CT image.

Fig.5(a) shows an example slice of the cost image for region term in PET image.

d) Boundary term: The boundary term measures the penalty of assigning different labels to the neighboring voxels u and v. We employ a gradient-based cost which has a similar form as the well-known graph cut method [23]. The boundary cost is described as following:

$$B_{uv} = -\log\left(1 - \exp\left(\frac{-|\nabla G_{PET}|^2(u,v)}{2\sigma_g^2}\right)\right), \quad (16)$$

where $|\nabla G_{PET}|^2(u,v)$ denotes the squared gradient magnitude between u and v, σ_g is a given Gaussian parameter.

3) Cost Function for CT: The energy function for CT comprises a data term $R_{u'}(f_{u'})$, a shape penalty term $S_{u'}(f_{u'})$ and a boundary term $B_{u'v'}(f_{u'}, f_{v'})$. The data term and the boundary term are derived from conventional graph cut energy term. The shape term is independent of image information. CT energy function has the following formulation.

$$E_{CT}(f) = \sum_{u' \in G_{CT}} \lambda_3(R_{u'}(f_{u'}) + S_{u'}(f_{u'}))$$
$$+ \sum_{(u',v') \in N_{CT}} \lambda_4 B_{u'v'}(f_{u'}, f_{v'}), \quad (17)$$

where λ_3, λ_4 is the scaling constant which maintains the role of the region cost, the shape term and the boundary term.

a) Data term: The hard region cost has the same form as that defined for PET. If voxel u' is in the interior of the pre-defined tumor region, $R_{u'}(f_{u'} = 1) = 0$ and $R_{u'}(f_{u'} = 0) = +\infty$. The background seed set is determined by the exterior area of the downhill region which we introduce in Section III-C-2-c. Similarly, $R_{u'}(f_{u'} = 0) = 0$ and $R_{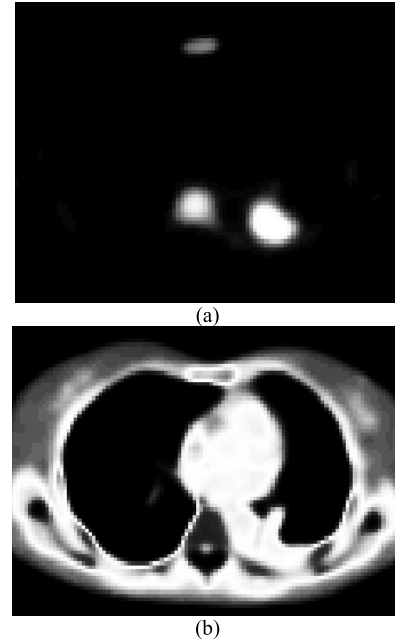u'}(f_{u'} = 1) = +\infty$ are defined for every voxel in the background set. For the area outside the background and foreground fields, the intensity distribution of CT image is assumed as the Gaussian Mixture Model [23]. Instead of being hard constraints, object seed sets are also used to compute the parameters of the Gaussian model. The mean intensity values of all voxels in pre-defined object are denoted by $\overline{g}$ and the corresponding standard deviation is σ.

$$R_{u'}(f_{u'} = 1) = -\log P(g_{u'}|f_{u'} = 1) \propto \frac{(g_{u'} - \overline{g})}{\sigma^2}, \quad (18)$$
$$R_{u'}(f_{u'} = 0) = -\log P(g_{u'}|f_{u'} = 0)$$
$$\propto -log(1 - exp(\frac{-(g_{u'} - \overline{g})^2}{\sigma^2})), \quad (19)$$

b) Shape term: The shape term is independent of image information [62], [63]. The region recognized by random walk is used as the shape prior to locate the tumor site. The distance from the current voxel to the model region is calculated and is considered as the penalty of assigning label $f = 1$ to voxel, the larger the distance, the larger the cost. The shape constraint function has the following form.

$$S_{u'}(f_{u'}) = 1 - \exp\left(-\frac{d(u', x_O)}{r_O}\right), \quad (20)$$

where $d(u', x_O)$ is the distance from voxel u' to the current shape x_O which is identified by random walk. If u' is inside object O, $d(u', x_O) = 0$, otherwise, $d(u', x_O)$ equals to the Euclidian distance from voxel u' to the center of the shape x_O. r_O is the radius of a circle. Fig.5(b) shows an example slice of the cost image for region term in CT image.

c) Boundary term: A gradient based function similar to that defined for PET is utilized, which takes the form

$$B_{u'v'} = -\log\left(1 - \exp\left(\frac{-|\nabla G_{CT}|^2(u',v')}{2\sigma_{g'}^2}\right)\right), \quad (21)$$

where $|\nabla G_{CT}|^2(u', v')$ denotes the squared gradient magnitude between u' and v'. $\sigma_{g'}$ are given parameters.

4) Context Function: To make the best incorporation of the information in PET and CT, a context term is introduced. The context energy function takes the form as follows [22]:

$$E_{context}(f) = p(1 - |N_u - N_{u'}|) + q, \qquad (22)$$

where p is a scaling constant, q is the penalty for an inconsistent segmentation. N_u and $N_{u'}$ are the normalization of the region cost in PET and CT images. The cost is linearly normalized between [0, 1]. The normalization is to make sure that if the two voxels in PET and CT images belong to the same label set (either to foreground or background), they will have similar region cost [22]. If a pair voxel (u, u') has similar region cost, a larger context cost will be assigned to penalize the inconsistency between PET and CT. The context cost enables our method to follow the prominent features form each modality and obtain two different volumes on PET and CT.

IV. EXPERIMENTS AND VALIDATION

In this section, the effectiveness of the proposed algorithm in delineating uptake regions from PET images was shown. The proposed method was carried out on 18 sets of PET-CT images for validation. For quantitative assessment, the segmentation performance on PET images was evaluated by comparing the computed results against the reference standard.

A. Datasets

Our co-segmentation approach was evaluated in a data set which consists of 18 3-D PET-CT images obtained from different patients with non-small cell lung cancer (NSCLC). For each slice of PET images, the reconstructed matrix size is $92 \times 92 \times 60$ with a voxel size $5.47 \times 5.47 \times 3.27$ mm^3. The reconstructed matrix size for each CT slice is $512 \times 512 \times 60$ with a voxel size $0.98 \times 0.98 \times 3.27$ mm^3. PET images were registered and upsampled using a linear interpolator to obtain one-to-one voxel correspondence between PET and CT images. The reference segmentations were obtained by two experts manually on the PET images by the guidance of the corresponding CT image. In this work, the segmentation can be done for multiple tumors. However, to guarantee the optimality of the algorithm, the segmentation is one by one.

B. Parameter Setting

In the experiments, the parameter was empirically employed for all analyzed datasets. For random walk segmentation, the weighting parameter β is set as 40. For the segmentation on PET, we set the maximum region cost as $T_{max} = 100000$, indicating that if the possibility a voxel belongs to the desired area is very small, the cost of labeling it as the target region is very large. In PET segmentation, the regional term plays a more important role than the boundary term so that we set $\lambda_1 = 1$ for region term. For the smoothness term, $\lambda_2 = 0.1$, $\sigma_g = 0.5$. For the SUV distribution term, $\varphi = 20\% \cdot S_{MAX}$, $\gamma = 4\% \cdot S_{MAX}$. For the 3D derivative cost term, the parameters for equation 11 are set as $\delta = 1$, $\sigma_1 = 1.5$. For the downhill term, μ is
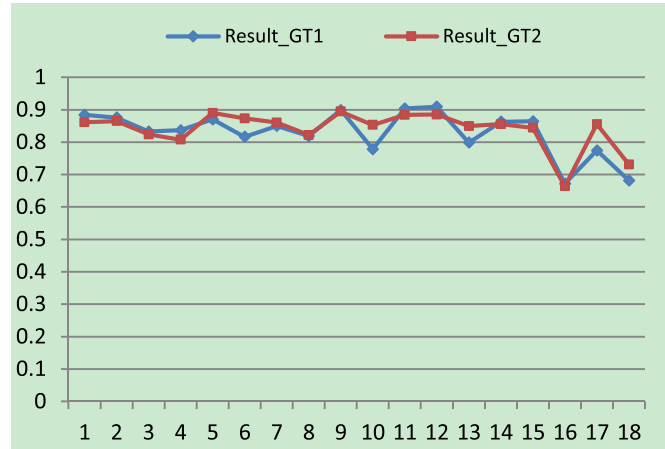

Fig. 6. The quantitative results for the segmentation results and two manual tumor contours.

set as 0.6. For the CT segmentation, the boundary term has a great impact on delineated results, thus we set $\lambda_3 = 1$ for the regional term. For the boundary term, $\lambda_4 = 5$, $\sigma_{g'} = 0.5$. In the context cost function, the scaling coefficient was set as $p = 0.2$, the inconsistent penalty was set as $q = 0.1$.

C. Evaluation of Segmentation

1) Evaluation Metrics: To measure the segmentation performance, Dice Similarity Coefficient (DSC) was used to evaluate the accuracy of the segmented result against the ground truth. DSC measures how the segmented volume matches the reference standard. We denote the segmented results and the ground truth by U_1 and U_2. The Dice Similarity Coefficient is computed as:

$$DSC(U_1, U_2) = 2 \cdot \frac{|U_1 \cap U_2|}{|U_1| + |U_2|}, \qquad (23)$$

2) Consistency Between Segmented Results and Manual Ground Truth: To demonstrate the consistency between the two manual ground truth, the DSC results were computed for the segmentation results and the two manual contours. The quantitative results are shown in Fig.6. In this work, we use the user2 as the reference standard.

3) Comparison With Graph Cut Solely on PET or CT: To determine the performance of co-segmentation of PET and CT images, we compare the proposed method with graph cut solely conducted on PET or CT images. The three methods are all applied to the 18 datasets with identical initialization. We have optimized parameters setting for each cost function in the three methods. DSC is computed to provide quantitative analysis. The quantitative evaluation of this comparison results is shown in Fig.7 and reports that the co-segmentation method outperforms the graph cut method conducted solely on PET or CT.

4) Comparison With Improved Graph Cut Co-Segmentation and Random Walk Method: In this paper, graph cut and random walk are combined together and a novel energy function for both PET and CT is devised. To evaluate the significance of the combination of the two methods, we compare the proposed
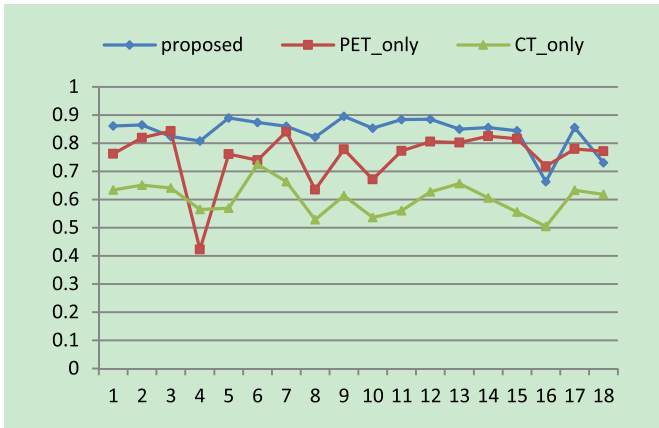
Fig. 7. Quantitative results and comparative performance evaluation based on the computed DSC values.
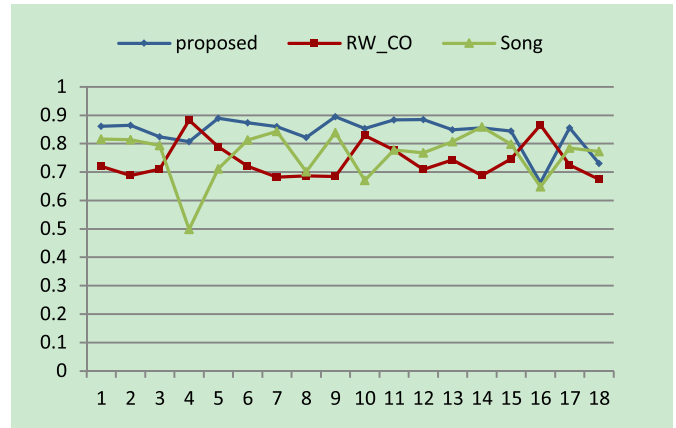

Fig. 9. Quantitative results for the proposed method compared to two related works, Song's GC-Cosegmentation method and Bagic's RW-Cosegmentation.
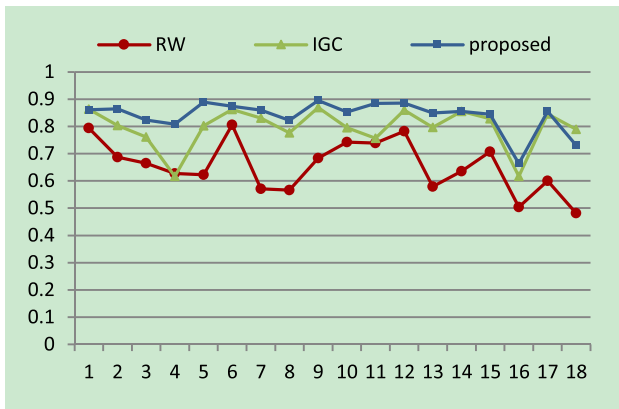

Fig. 8. Quantitative results for the proposed method compared to improved graph cut (IGC) and random walk method. The comparative performance evaluation is based on the computed DSC values.
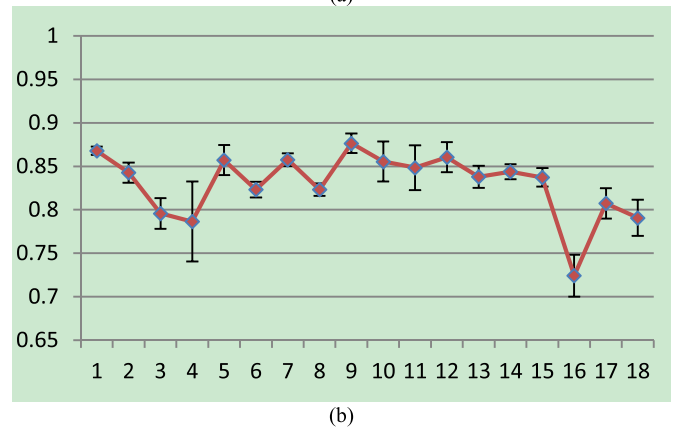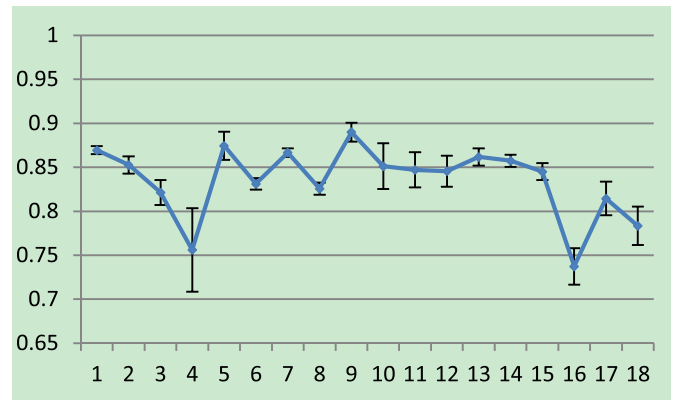

(a)

(b)

Fig. 10. Quantitative results for the proposed method using different initialization. The Monte-Carlo simulation was operated 100 times for 5 and 3 selected seeds. (a) mean DSC and STD for 5 seeds. (b) mean DSC and STD for 3 seeds.

method with random walk (RW) conducted solely on PET images and the improved graph cut co-segmentation method (denoted by IGC) which has the novel energy regularization but without the random walk method. In this comparison, the same foreground and background seed sets are used as initialization. For quantitative evaluation, the results are displayed in Fig.8, indicating that the combination of random walk and graph cut has great significance in the segmentation of the tumor on PET and CT.

5) Comparison With the Related Works: The closely related work to our method is Song *et al*. [22] and Bagic *et al*. [18]. The comparison experiments were made with the two algorithms. Comparison to Song's method can demonstrate the effectiveness of the proposed new energy representation. Quantitative results were displayed on Fig.9, indicating that our algorithm has an excellent performance. TABLE I shows the mean DSC and STD for the proposed method and the six comparative methods. Fig.12 shows the segmentation results for six compared methods. The illustrative results for the proposed method are shown on Fig.13.

6) Robustness to Seed Initialization: To assess the reliability of the proposed method to the location and quantity of the seed points, a Monte-Carlo simulation is used to produce seeds randomly. The seed number is set as 5 voxels and 3voxels.

The Monte-Carlo simulation is operated 100 times for each group. For each patient, the average DSC and standard deviation were computed. The quantitative results are displayed in Fig.10 and indicate the stability of the proposed method to seed initialization. TABLE II. shows the average DSC and STD for each group.

7) Sensitivity to Parameter Setting: In this paper, there are many parameters that would affect the performance of

TABLE I

QUANTITATIVE DSC RATE USING THE PROPOSED METHOD COMPARED
WITH SIX OTHER METHODS: GRAPH UCT SOLELY USING PET, GRAPH
CUT SOLELY USING CT, RANDOM WALK METHOD, SONG'S METHOD,
IMPROVED GRAPH CUT, RW-COSEGMENTATION. RESULTS ARE
REPORTED AS MEAN±STANDARD DEVIATION

Rank	Methods	DSC
1	PET only	0.753±0.099
2	CT only	0.605±0.056
3	RW	0.656±0.096
4	Song	0.762±0.088
5	IGC	0.796±0.074
6	RW-CO	0.740±0.064
7	Our method	0.840±0.058

TABLE II

MEAN DSC AND STANDARD DEVIATION FOR DIFFERENT INITIALIZATION

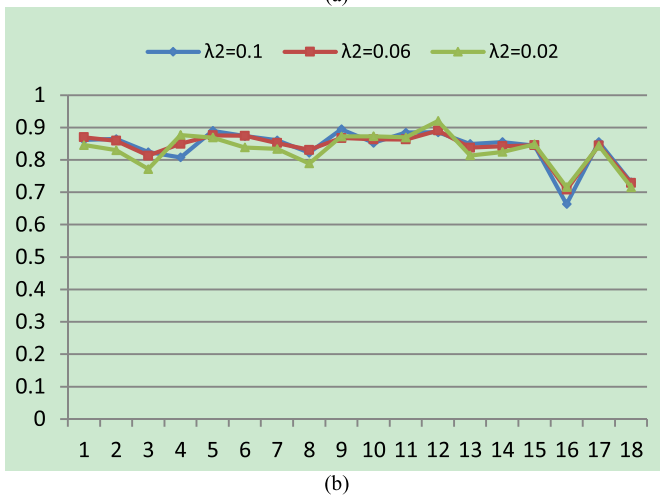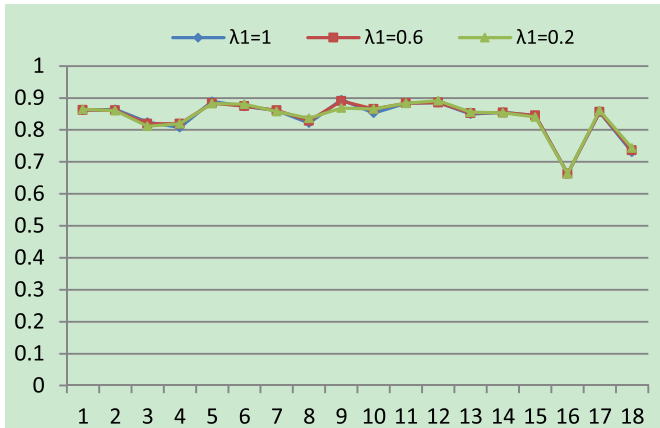|	5 Seeds	3 Seeds
MEAN DSC	0.835	0.830
STD	0.0151	0.0163

Fig. 11. Quantitative results for the proposed method using different parameter setting on PET energy function. (a) λ_1 for the data term is set as 1.0, 0.6, 0.2 . (b) λ_2 for the boundary term is set as 0.1, 0.06, 0.02.
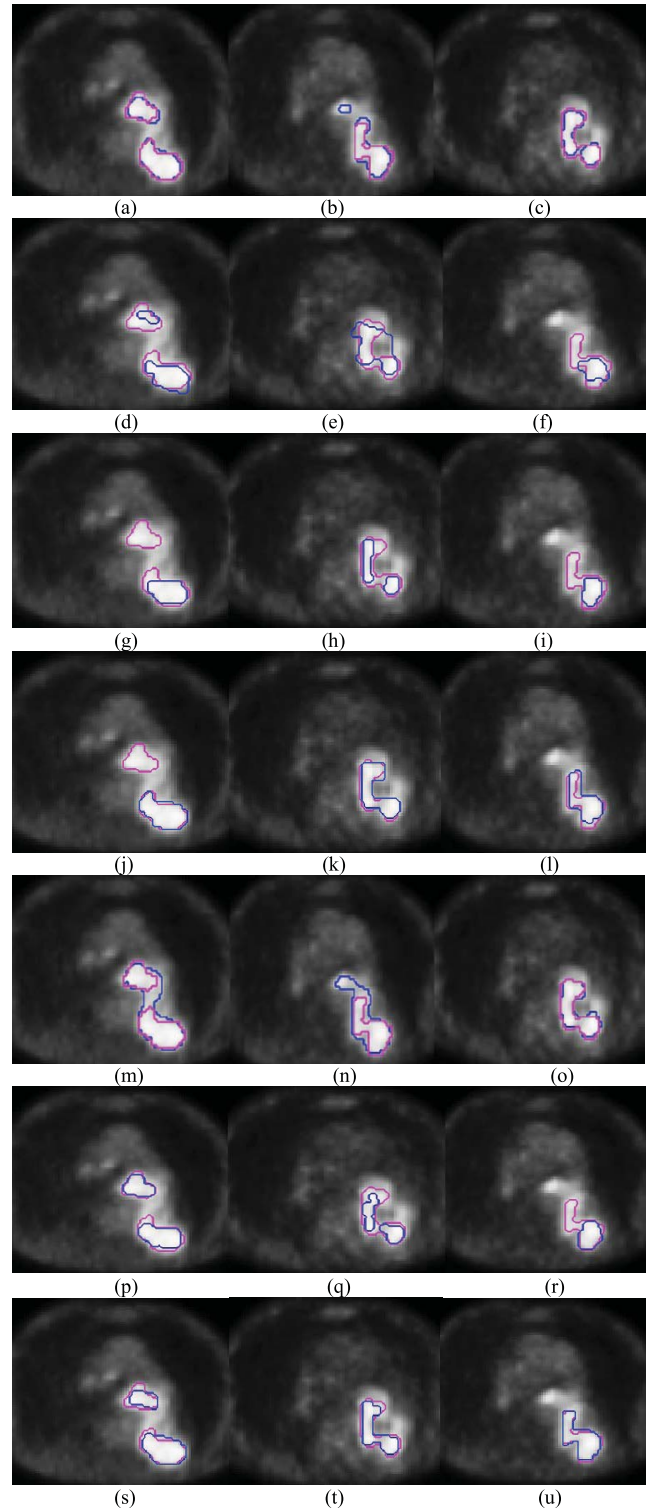

Fig. 12. Three different comparative segmentation results of lesions are shown in each column. The segmentation results on PET (blue) and ground truth (red) are overlaid (a)–(c) the results by graph cut conducted solely on PET images. (d)–(f) segmentation results conducted solely on CT images (g)–(i) segmentation results by random walk (j)–(l) improved co-segmentation graph cut method (IGC). (m)–(o) traditional co-segmentation graph cut method (Song's method). (p)–(r) the results conducted by random walk co-segmentation. (s)–(u) segmentation results conducted by our proposed method.

the algorithm. To demonstrate the sensitivity of our method to the parameter, we changed the parameters on the energy function E_{PET}, λ_1 for the data term and λ_2 for the boundary term. The value for λ_1 is set as 1.0, 0.6, 0.2 and the other parameters remain the same. The quantitative results are shown in Fig.11(a). The value for λ_2 is also set as 0.1, 0.06, 0.02.
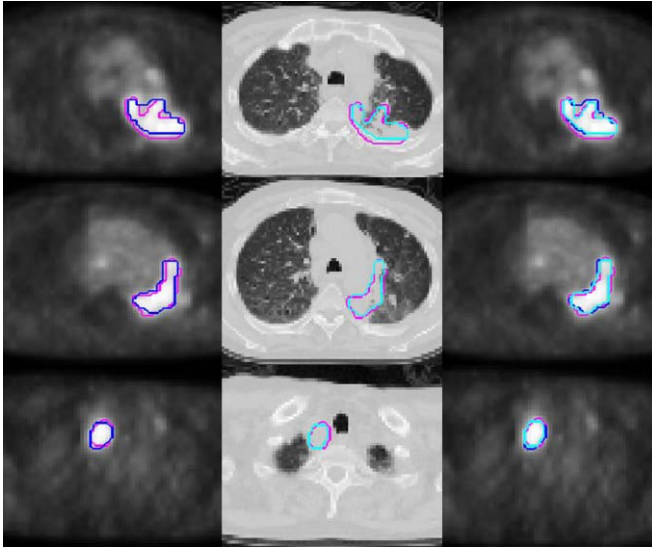
Fig. 13.   Three typical segmentation examples are shown in each column. First colun: our proposed co-segmentation results on PET (blue) and ground truth (red) are overlaid. Second column: co-segmentation from CT (light blue) and ground truth (red). Third column: all segmentations and ground truth are overlaid on the PET images.

The results are displayed in Fig.11(b). The quantitative results show the proposed method is quite robust to the setting of the parameters.

D. Execution Time

Our algorithm was implemented in C++ on a Windows7 workstation (3.1GHz, 64GB memory). For each dataset, our algorithm took about 1min (average time).

V. Conclusion

In this paper, we aim to segment the tumor simultaneously on PET and CT by effectively integrating the physiological information from PET and anatomical information from CT. The key novelty of our method is the incorporation of random walk and graph cut method and the cost function we design for graph cut segmentation on PET and CT. The integration of the two methods can avoid the small cut problem in graph cut and has good performance in capturing fuzzy boundary of the tumor on PET images. The novel energy function we proposed effectively utilizes the features from both PET and CT images. Each feature has contributions to tumor segmentation. The SUV distribution feature makes our method perform well on segmentation of both homogeneous and heterogeneous tumor. The downhill feature can extract the surrounding tissues with high uptakes similar to tumor SUV and its exterior can be used as the background seeds for CT segmentation. The 3D local structure enhancement feature has the advantage of specifying the blob-like tumor objects. The shape term in the energy function for CT segmentation helps locate the tumor site. The results demonstrated the effectiveness of the proposed novel energy functions when compared our method to the traditional graph cut method. The significant improvement is achieved when compared to other segmentation methods.

VI. Discussion

A. Significance of the Combination of Random Walk and Graph Cut

The common problem in the graph cut method is the small cut behavior [65]. In the paper, the proposed algorithm is not suffering from the problem because the random walk method provides smart seeds for graph cut method. Since random walk has advantage in capturing weak object boundaries, the combination makes it significant in dealing with fuzzy boundaries of tumor. And in our dataset, the cancer area is in general small compared to the image.

B. Significance of the Novel Function

In this paper, graph cut method is improved by the introduction of the novel energy function. The downhill function takes the advantage of the feature of the tumor intensity distribution and the distance to the tumor site. This function helps to locate the tumor and extract the surrounding tissues which have similar intensity distribution to tumor. CT lacks metabolism information and has low contrast, so that it is difficult to distinguish between the disease areas and the normal tissues. To locate the tumor site in CT image, we introduce a shape constraint function which utilizes the prior information of the tumor as shape prior to constrain the tumor region growing. This function translates the Euclidean distance to the cost, the larger the distance from the voxel to the shape, the larger the cost.

C. Further Improvements

The identification of the foreground and background seed points can be automated. Bagic et al. [18] have developed a seed automatic detection algorithm. The algorithm proposed in [18] set a threshold for the PET SUV to define the object seeds first. Then neighboring voxels are searched to find voxels with SUVs lower than another threshold. Those voxels are defined as foreground and background seeds. However, the heart and liver with high uptake SUV which is similar to the tumor intensity will be wrong detected as the foreground seeds, leading to a wrong guidance to the segmentation. In the future, the detailed information of the lung structure will be extracted from PET and CT images. The location and the size of the organs are contained in the structure information. This structure information will facilitate the identification of the foreground seeds and do not yield ambiguity.

Multi-modality has become a standard method in clinical pathological analysis, each kind of the imaging techniques capture different characteristics of human body. Although the co-segmentation makes use of the superior tumor contrast from PET images and the exquisite anatomical information from CT images, PET and CT cannot provide enough complementary information to each other. In the future, we plan to apply our framework to joint segmentation of MRI, PET and CT. The combination of the three modalities, and even more modalities, will produce a more accurate segmentation tumor results.

The anisotropic diffusion filter used in the paper considers the noise of PET images as Gaussian distribution. It may

result in loss of poor resolution and increased blurring of PET images. If the quantification is needed after segmentation, then a proper denoising method should be chosen. The generalized Anscombe's transformation (GAT) method [66] can be used to stabilize the PET noise. And the trilateral filtering can be used to preserve the boundaries of the structures while smoothing the noisy regions and avoid significant loss of quantitative information. The trilateral filtering, considering the noise distribution in PET images as Poisson-Gaussian mixed can effectively remove signal-dependent noise in the PET images.

ACKNOWLEDGMENT

REFERENCES

[1] B. W. Stewart and C. P. Wild, *World Cancer Report 2014*. Lyon, France: International Agency for Research on Cancer, 2014.

[2] W. J. Curran, Jr., *et al.*, "Sequential vs concurrent chemoradiation for stage III non–small cell lung cancer: Randomized phase III trial RTOG 9410," *J. Nat. Cancer Inst.*, vol. 103, no. 19, pp. 1452–1460, 2011.

[3] K. Suzuki *et al.*, "A prospective radiological study of thin-section computed tomography to predict pathological noninvasiveness in peripheral clinical IA lung cancer (Japan clinical oncology group 0201)," *J. Thoracic Oncol.*, vol. 6, no. 4, pp. 751–756, 2011.

[4] T. Koike, T. Koike, Y. Yamato, K. Yoshiya, and S.-I. Toyabe, "Prognostic predictors in non-small cell lung cancer patients undergoing intentional segmentectomy," *Ann. Thoracic Surgery*, vol. 93, no. 6, pp. 1788–1794, Jun. 2012.

[5] M. Okada *et al.*, "Multicenter analysis of high-resolution computed tomography and positron emission tomography/computed tomography findings to choose therapeutic strategies for clinical stage IA lung adenocarcinoma," *J. Thoracic Cardiovascular Surgery*, vol. 141, no. 6, pp. 1384–1391, Jun. 2011.

[6] A. van Baardwijk *et al.*, "The maximum uptake of ^{18}F-deoxyglucose on positron emission tomography scan correlates with survival, hypoxia inducible factor-1a and GLUT-1 in non-small cell lung cancer," *Eur. J. Cancer*, vol. 43, no. 9, pp. 1392–1398, Jun. 2007.

[7] W. van Elmpt *et al.*, "Characterization of tumor heterogeneity using dynamic contrast enhanced CT and FDG-PET in non-small cell lung cancer," *Radiotherapy Oncol.*, vol. 109, no. 1, pp. 65–70, Oct. 2013.

[8] J. Bradley *et al.*, "Impact of FDG-PET on radiation therapy volume delineation in non–small-cell lung cancer," *Int. J. Radiation Oncol. Biol. Phys.*, vol. 59, no. 1, pp. 78–86, May 2004.

[9] J. B. Davis, B. Reiner, M. Huser, C. Burger, G. Székely, and I. F. Ciernik, "Assessment of ^{18}F PET signals for automatic target volume definition in radiotherapy treatment planning," *Radiotherapy Oncol.*, vol. 80, pp. 43–50, Jul. 2006.

[10] Y. E. Erdi *et al.*, "Radiotherapy treatment planning for patients with non-small cell lung cancer using positron emission tomography (PET)," *Radiotherapy Oncol.*, vol. 62, no. 1, pp. 51–60, Jan. 2002.

[11] R. Boellaard, N. C. Krak, O. S. Hoekstra, and A. A. Lammertsma, "Effects of noise, image resolution, and ROI definition on the accuracy of standard uptake values: A simulation study," *J. Nucl. Med.*, vol. 45, no. 9, pp. 1519–1527, 2004.

[12] A. van Baardwijk *et al.*, "PET-CT–based auto-contouring in non–small-cell lung cancer correlates with pathology and reduces interobserver variability in the delineation of the primary tumor and involved nodal volumes," *Int. J. Radiat. Oncol. Biol. Phys.*, vol. 68, no. 3, pp. 771–778, Jul. 2007.

[13] C. Greco, K. Rosenzweig, G. L. Cascini, and O. Tamburrini, "Current status of PET/CT for tumour volume definition in radiotherapy treatment planning for non-small cell lung cancer (NSCLC)," *Lung Cancer*, vol. 57, no. 2, pp. 125–134, Aug. 2007.

[14] R. J. H. M. Steenbakkers *et al.*, "Reduction of observer variation using matched CT-PET for lung cancer delineation: A three-dimensional analysis," *Int. J. Radiat. Oncol., Biol., Phys.*, vol. 64, no. 2, pp. 435–448, Feb. 2006.

[15] J. Erasmus *et al.*, "Interobserver and intraobserver variability in measurement of non–small–cell carcinoma lung lesions: Implications for assessment of tumor response," *J. Clin. Oncol.*, vol. 21, no. 13, pp. 2574–2582, 2003.

[16] J. L. Fox *et al.*, "Does registration of PET and planning CT images decrease interobserver and intraobserver variation in delineating tumor volumes for non–small-cell lung cancer?" *Int. J. Radiat. Oncol., Biol., Phys.*, vol. 62, no. 1, pp. 70–75, May 2005.

[17] M. T. Munley *et al.*, "Multimodality nuclear medicine imaging in three-dimensional radiation treatment planning for lung cancer: Challenges and prospects," *Lung Cancer*, vol. 23, no. 2, pp. 105–114, Feb. 1999.

[18] U. Bagci *et al.*, "Joint segmentation of anatomical and functional images: Applications in quantification of lesions from PET, PET-CT, MRI-PET, and MRI-PET-CT images," *Med. Image Anal.*, vol. 17, no. 8, pp. 929–945, Dec. 2013.

[19] U. Bagci, J. K. Udupa, J. Yao, and D. J. Mollura, "Co-segmentation of functional and anatomical images," in *Proc. Int. Conf. Med. Image Comput. Comput. Assist. Intervent.*, 2012, pp. 459–467.

[20] D. Han *et al.*, "Globally optimal tumor segmentation in PET-CT images: A graph-based co-segmentation method," in *Information Processing in Medical Imaging*. Berlin, Germany: Springer-Verlag, 2011, pp. 245–256.

[21] X. Wang *et al.*, "Lung tumor delineation based on novel tumor-background likelihood models in PET-CT images," *IEEE Trans. Nucl. Sci.*, vol. 61, no. 1, pp. 218–224, Feb. 2014.

[22] Q. Song *et al.*, "Optimal co-segmentation of tumor in PET-CT images with context information," *IEEE Trans. Med. Imag.*, vol. 32, no. 9, pp. 1685–1697, Sep. 2013.

[23] Y. Y. Boykov and M.-P. Jolly, "Interactive graph cuts for optimal boundary & region segmentation of objects in N-D images," in *Proc. IEEE Int. Conf. Comput. Vis.*, Jul. 2001, pp. 105–112.

[24] Y. Boykov and O. Veksler, "Graph cuts in vision and graphics: Theories and applications," in *Handbook of Mathematical Models in Computer Vision*. Berlin, Germany: Springer-Verlag, 2006.

[25] Y. Boykov and V. Kolmogorov, "An experimental comparison of min-cut/max-flow algorithms for energy minimization in vision," *IEEE Trans. Pattern Anal. Mach. Intell.*, vol. 28, no. 9, pp. 1124–1137, Sep. 2004.

[26] Y. Boykov, O. Veksler, and R. Zabih, "Fast approximate energy minimization via graph cuts," *IEEE Trans. Pattern Anal. Mach. Intell.*, vol. 23, no. 11, pp. 1222–1239, Nov. 2001.

[27] Y. Boykov and G. Funka-Lea, "Graph cuts and efficient N-D image segmentation," *Int. J. Comput. Vis.*, vol. 70, no. 2, pp. 109–131, Nov. 2006.

[28] L. Grady, "Random walks for image segmentation," *IEEE Trans. Pattern Anal. Mach. Intell.*, vol. 28, no. 11, pp. 1768–1783, Nov. 2006.

[29] L. Grady, T. Schiwietz, S. Aharon, and R. Westermann, "Random walks for interactive organ segmentation in two and three dimensions: Implementation and validation," in *Proc. 8th Int. Conf. Med. Image Comput. Comput. Assisted Intervent.*, Palm Springs, CA, USA, 2005, pp. 773–780.

[30] A. K. Sinop and L. Grady, "A seeded image segmentation framework unifying graph cuts and random walker which yields a new algorithm," in *Proc. ICCV*, Rio de Janeiro, Brazil, Oct. 2007, pp. 1–8.

[31] Y. E. Erdi *et al.*, "Segmentation of lung lesion volume by adaptive positron emission tomography image thresholding," *Cancer*, vol. 80, no. S12, pp. 2505–2509, Dec. 1997.

[32] C. B. Caldwell, K. Mah, M. Skinner, and C. E. Danjoux, "Can PET provide the 3D extent of tumor motion for individualized internal target volumes? A phantom study of the limitations of CT and the promise of PET," *Int. J. Radiat. Oncol., Biol., Phys.*, vol. 55, no. 5, pp. 1381–1393, Apr. 2003.

[33] L. Drever, D. Robinson, A. McEwan, and W. Roa, "A local contrast based approach to threshold segmentation for PET target volume delineation," *Med. Phys.*, vol. 33, no. 6, p. 1583, 2006.

[34] L. Drever, W. Roa, A. McEwan, and D. Robinson, "Iterative threshold segmentation for PET target volume delineation," *Med. Phys.*, vol. 34, no. 4, p. 1253, 2007.

[35] W. Jentzen, L. Freudenberg, E. G. Eising, M. Heinze, W. Brandau, and A. Bockisch, "Segmentation of PET volumes by iterative image thresholding," *J. Nucl. Med.*, vol. 48, no. 1, pp. 108–114, Jan. 2007.

[36] M. Brambilla, R. Matheoud, C. Secco, G. Loi, M. Krengli, and E. Inglese, "Threshold segmentation for PET target volume delineation in radiation treatment planning: The role of target-to-background ratio and target size," *Med. Phys.*, vol. 35, no. 4, pp. 1207–1213, 2008.

[37] S. A. Nehmeh *et al.*, "An iterative technique to segment PET lesions using a Monte Carlo based mathematical model," *Med. Phys.*, vol. 36, no. 10, pp. 4803–4809, 2009.

[38] K.-P. Wong, D. Feng, S. R. Meikle, and M. J. Fulham, "Segmentation of dynamic PET images using cluster analysis," *IEEE Trans. Nucl. Sci.*, vol. 49, no. 1, pp. 200–207, Feb. 2002.

[39] X. Geets, J. A. Lee, A. Bol, M. Lonneux, and V. Grégoire, "A gradient-based method for segmenting FDG-PET images: Methodology and validation," *Eur. J. Nucl. Med. Molecular Imag.*, vol. 34, no. 9, pp. 1427–1438, Sep. 2007.

[40] M. Wanet *et al.*, "Gradient-based delineation of the primary GTV on FDG-PET in non-small cell lung cancer: A comparison with threshold-based approaches, CT and surgical specimens," *Radiotherapy Oncol.*, vol. 98, no. 1, pp. 117–125, 2011.

[41] S. Belhassen and H. Zaidi, "A novel fuzzy C-means algorithm for unsupervised heterogeneous tumor quantification in PET," *Med. Phys.*, vol. 37, no. 3, pp. 1309–1324, 2010.

[42] M. S. Sharif, M. Abbod, A. Amira, and H. Zaidi, "Artificial neural network-based system for PET volume segmentation," *J. Biomed. Imag.*, vol. 2010, p. 4, Jan. 2010.

[43] G. V. Saradhi *et al.*, "A framework for automated tumor detection in thoracic FDG pet images using texture-based features," in *Proc. IEEE Int. Symp. Biomed. Imag., From Nano Macro (ISBI)*, Jun./Jul. 2009, pp. 97–100.

[44] P. E. Galavis, C. Hollensen, N. Jallow, B. Paliwal, and R. Jeraj, "Variability of textural features in FDG PET images due to different acquisition modes and reconstruction parameters," *Acta Oncol.*, vol. 49, no. 7, pp. 1012–1016, 2010.

[45] S. Chicklore, V. Goh, M. Siddique, A. Roy, P. K. Marsden, and G. J. R. Cook, "Quantifying tumour heterogeneity in 18F-FDG PET/CT imaging by texture analysis," *Eur. J. Nucl. Med. Molecular Imag.*, vol. 40, no. 1, pp. 133–140, 2013.

[46] H. Guan *et al.*, "Automatic hot spot detection and segmentation in whole body FDG-PET images," in *Proc. IEEE Int. Conf. Image Process.*, Oct. 2006, pp. 85–88.

[47] D. W. G. Montgomery, A. Amira, and H. Zaidi, "Fully automated segmentation of oncological PET volumes using a combined multi-scale and statistical model," *Med. Phys.*, vol. 34, no. 2, pp. 722–736, 2007.

[48] M. Aristophanous, B. C. Penney, M. K. Martel, and C. A. Pelizzari, "A Gaussian mixture model for definition of lung tumor volumes in positron emission tomography," *Med. Phys.*, vol. 34, no. 11, pp. 4223–4235, 2007.

[49] C. Ballangan, X. Wang, M. Fulham, S. Eberl, Y. Yin, and D. Feng, "Automated delineation of lung tumors in PET images based on monotonicity and a tumor-customized criterion," *IEEE Trans. Inf. Technol. Biomed.*, vol. 15, no. 5, pp. 691–702, Sep. 2011.

[50] A. Dewalle-Vignion, N. Betrouni, R. Lopes, D. Huglo, S. Stute, and M. Vermandel, "A new method for volume segmentation of PET images, based on possibility theory," *IEEE Trans. Med. Imag.*, vol. 30, no. 2, pp. 409–423, Feb. 2011.

[51] U. Bagci, J. Yao, J. Caban, E. Turkbey, O. Aras, and D. J. Mollura, "A graph-theoretic approach for segmentation of PET images," in *Proc. Annu. Int. Conf. IEEE Eng. Med. Biol. Soc. (EMBS)*, Aug./Sep. 2011, pp. 8479–8482.

[52] C. Ballangan, X. Wang, M. Fulham, S. Eberl, and D. Feng, "Lung tumor segmentation in PET images using graph cuts," *Comput. Methods Programs Biomed.*, vol. 109, no. 3, pp. 260–268, Mar. 2013.

[53] J.-M. Kuhnigk *et al.*, "Morphological segmentation and partial volume analysis for volumetry of solid pulmonary lesions in thoracic CT scans," *IEEE Trans. Med. Imag.*, vol. 25, no. 4, pp. 417–434, Apr. 2006.

[54] D. Wu *et al.*, "Stratified learning of local anatomical context for lung nodules in CT images," in *Proc. IEEE Conf. Comput. Vis. Pattern Recognit. (CVPR)*, Jun. 2010, pp. 2791–2798.

[55] Y. Tao *et al.*, "Multi-level ground glass nodule detection and segmentation in CT lung images," in *Medical Image Computing and Computer-Assisted Intervention—MICCAI*. Berlin, Germany: Springer-Verlag, 2009, pp. 715–723.

[56] Y. Gu *et al.*, "Automated delineation of lung tumors from CT images using a single click ensemble segmentation approach," *Pattern Recognit.*, vol. 46, no. 3, pp. 692–702, Mar. 2013.

[57] I. Jafar, H. Ying, A. F. Shields, and O. Muzik, "Computerized detection of lung tumors in PET/CT images," in *Proc. 28th Annu. Int. Conf. Eng. Med. Biol. Soc. (EMBS)*, Aug./Sep. 2006, pp. 2320–2323.

[58] C. Ballangan, X. Wang, D. Feng, S. Eberl, and M. Fulham, "Lung segmentation and tumor detection from CT thorax volumes of FDG PET-CT scans by template registration and incorporation of functional information," in *Proc. IEEE Nucl. Sci. Symp. Conf. Rec. (NSS)*, Oct. 2008, pp. 5349–5353.

[59] Y. Guo *et al.*, "Automatic lung tumor segmentation on PET/CT images using fuzzy Markov random field model," *Comput. Math. Methods Med.*, vol. 2014, May 2014, Art. ID 401201.

[60] H. Zaidi and I. El Naqa, "PET-guided delineation of radiation therapy treatment volumes: A survey of image segmentation techniques," *Eur. J. Nucl. Med. Molecular Imag.*, vol. 37, no. 11, pp. 2165–2187, Nov. 2010.

[61] Y. Sato *et al.*, "Tissue classification based on 3D local intensity structures for volume rendering," *IEEE Trans. Vis. Comput. Graphics*, vol. 6, no. 2, pp. 160–180, Apr./Jun. 2000.

[62] X. Chen, J. K. Udupa, U. Bagci, Y. Zhuge, and J. Yao, "Medical image segmentation by combining graph cuts and oriented active appearance models," *IEEE Trans. Image Process.*, vol. 21, no. 4, pp. 2035–2046, Apr. 2012.

[63] X. Chen *et al.*, "A framework of whole heart extracellular volume fraction estimation for low-dose cardiac CT images," *IEEE Trans. Inf. Technol. Biomed.*, vol. 16, no. 5, pp. 842–851, Sep. 2012.

[64] T. Fawcett, "An introduction to ROC analysis," *Pattern Recognit. Lett.*, vol. 27, no. 8, pp. 861–874, Jun. 2006.

[65] Z. Wu and R. Leahy, "An optimal graph theoretic approach to data clustering: Theory and its application to image segmentation," *IEEE Trans. Pattern Anal. Mach. Intell.*, vol. 15, no. 11, pp. 1101–1113, Nov. 1993.

[66] A. Mansoor, U. Bagci, and D. J. Mollura, "Optimally stabilized PET image denoising using trilateral filtering," in *Medical Image Computing and Computer-Assisted Intervention—MICCAI*. New York, NY, USA: Springer-Verlag, 2014, pp. 130–137.

Wei Ju received the B.E. degree in electronics and information engineering and the master's degree in electronics and information engineering from Soochow University, China, in 2012 and 2015, respectively. Her current research interests include medical data segmentation, medical image analysis, and pattern recognition.
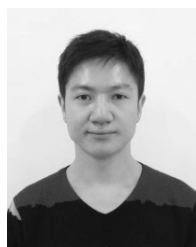
Deihui Xiang received the B.E. degree in automation from Sichuan University, Sichuan, China, in 2007, and the Ph.D. degree from the Institute of Automation, Chinese Academy of Sciences, Beijing, China, in 2012. He is currently an Associate Professor with the School of Electronics and Information Engineering, Soochow University, Jiangsu, China. His current research interests include medical image analysis, computer vision, medical data visualization, and pattern recognition.

Bin Zhang received the Ph.D. degree from the School of Radiation Medicine and Protection, Medical College, Soochow University, in 2009. He is currently an Associate Chief Physician and Associate Professor with the Department of Nuclear Medicine, First Affiliated Hospital, Soochow University. His research mainly focuses on molecular imaging. He has authored over 30 papers in this field.

Lirong Wang received the Ph.D. degree from the Department of Communication Engineering, Jilin University, in 2006. She is currently a Professor with the School of Electronics and Information Engineering, Soochow University. Her research mainly focuses on information processing. She has authored over 30 papers in this field.

Ivica Kopriva (SM'15) received the Ph.D. degree from the Faculty of Electrical Engineering and Computing, University of Zagreb, in 1998, with a minor in blind source separation. From 2001 to 2005, he was a Research Scientist and Senior Research Scientist with the Department of Electrical and Computer Engineering, The George Washington University, Washington, DC, USA. Since 2006, he has been a Senior Scientist with the Ruder Bošković Institute, Zagreb, Croatia. He has authored over 40 papers in internationally recognized journals and holds three U.S. patents. He has co-authored the research monograph, such as *Kernel Based Algorithms for Mining Huge Data Sets: Supervised, Semi-Supervised and Unsupervised Learning* (Springer, 2006) in computational intelligence. His research interests are related to development of algorithms for unsupervised learning with applications in biomedical image analysis, chemometrics, and bioinformatics. He is a Senior Member of OSA.

Xinjian Chen received the Ph.D. degree from the Center for Biometrics and Security Research, Key Laboratory of Complex Systems and Intelligence Science, Institute of Automation, Chinese Academy of Sciences, Beijing, China, in 2006. After completing the graduation, he joined Microsoft Research Asia, where he was involved in research on handwriting recognition. From 2008 to 2012, he conducted the Post-Doctoral Research at several prestigious groups, such as the Medical Image Processing Group, University of Pennsylvania, the Department of Radiology and Image Sciences, National Institutes of Health, and the Department of Electrical and Computer Engineering, University of Iowa. In 2012, he joined the School of Electrical and Information Engineering, Soochow University, as a Full Professor. He has authored over 70 high quality international journal/conference papers. His research interests include medical image processing and analysis, pattern recognition, machine learning, and their applications. He is a Distinguished Professor with Soochow University, and serves as the Director of the University Level Laboratory–Medical Image Processing, Analysis and Visualization Laboratory.